

# Influence of Transformation Temperature on the High-Cycle Fatigue Performance of Carbide-Bearing and Carbide-Free Bainite

Oguz Gulbay,\* Marc Ackermann, Alexander Gramlich, Ali Riza Durmaz, Ingo Steinbach, and Ulrich Krupp

This study investigates the high-cycle-fatigue (HCF) behavior of carbide-bearing bainite (CBB) and carbide-free bainite (CFB) fabricated at different transformation temperatures. The fatigue limit of each material is determined via staircase method using a 1 kHz resonant testing machine. A new load increase test is proposed as an efficient alternative to estimate the fatigue limit in HCF regimes. The assessment of the fatigue behavior is accompanied by data-driven microstructural analyses via state-of-the-art computer vision tools. The analyses reveal that the finer carbide distribution, which is obtained at lower transformation temperature, enhances the overall performance of CBB. Electron backscatter diffraction (EBSD) measurements of CFB before and after tensile testing evidence the transformation of retained austenite (RA) to martensite during deformation. The finer film-like and stable RAs, which are promoted via reduction in transformation temperature, enhance the HCF properties by absorbing the energy required for fatigue crack propagation through improved transformation-induced plasticity. However, blocky unstable RA and/or martensite-austenite (MA) islands at prior austenite grain boundaries deteriorate the HCF properties of high-temperature CFB. Furthermore, unindexed regions in EBSD maps are effectively used to differentiate the MA islands of CFB, as validated by scanning electron microscopy (SEM) images and deep learning-based MA island segmentation.

and components, which consecutively increases the circularity of the steel industry.<sup>[1]</sup> Bainitic steels with cost-effective alloying concepts have attracted significant research attention to fulfil the requirements of many industrial applications. The performance of bainitic steels is highly related to the microstructural constituents and their morphology, which can be tailored by the chemical composition and processing parameters. In general, bainitic steels can be divided into two subgroups based on their microstructural constituents: carbide-bearing bainite (CBB) and carbide-free bainite (CFB). If there is no kinetic hindrance, then at higher temperatures bainitic steel may experience carbide precipitation (mostly cementite) in between bainitic ferrite (BF) plates. At lower temperatures, some of the carbon can be trapped and/or precipitated in supersaturated ferrite due to lower diffusion, leading to reduced amount of carbon partitioning into surrounding austenite, therefore, finer carbide precipitation between and within the BF plates.<sup>[2,3]</sup> In contrast, by the addition of silicon

(>1 wt%), retained austenite (RA) can be introduced as secondary phase.<sup>[4,5]</sup> The low solubility of silicon in cementite hinders cementite precipitation. This enables carbon diffusion from ferrite to austenite during phase transformation, which results in stabilization of the austenite.<sup>[6,7]</sup> Commonly, RA exhibits


## 1. Introduction

The development of new steels with good mechanical properties and high-fatigue resistance is critical for various industries because it improves the longevity and reliability of structures

O. Gulbay, M. Ackermann, A. Gramlich, U. Krupp  
Steel Institute  
RWTH Aachen University  
52072 Aachen, Germany  
E-mail: oguz.gulbay@iehk.rwth-aachen.de

A. R. Durmaz  
Meso and Micromechanics  
Fraunhofer Institute for Mechanics of Materials IWM  
79108 Freiburg, Germany

I. Steinbach  
Interdisciplinary Center for Advanced Material Simulations  
Ruhr Universität Bochum  
44801 Bochum, Germany

 The ORCID identification number(s) for the author(s) of this article can be found under <https://doi.org/10.1002/srin.202300238>.

© 2023 The Authors. Steel Research International published by Wiley-VCH GmbH. This is an open access article under the terms of the Creative Commons Attribution-NonCommercial-NoDerivs License, which permits use and distribution in any medium, provided the original work is properly cited, the use is non-commercial and no modifications or adaptations are made.

DOI: 10.1002/srin.202300238

film-like morphology between BF plates with a higher stability or blocky morphology with a lower stability.<sup>[4]</sup> Depending on the stability of austenite that varies with local carbon concentration, size, and morphology, some part of it may transform to martensite during cooling and form a complex structure called martensite-austenite (MA) islands.<sup>[8–10]</sup> The RA may transform to martensite through transformation-induced plasticity (TRIP) effect during deformation, leading to enhanced performance of the steel under static,<sup>[10,11]</sup> and cyclic loading<sup>[12,13]</sup> conditions. According to the incomplete-reaction phenomenon ( $T_0$  concept), the reduction in transformation temperature results in more diffusionless bainite transformation until a critical carbon concentration is reached, in which the free energy of BF is no longer less than that of austenite.<sup>[14]</sup> Therefore, at lower transformation temperatures, in addition to refinement of microstructural constituents, fraction, size, morphology, chemical composition, and stability of RA can also be altered.<sup>[12,15]</sup> Therefore, designing bainitic steels requires understanding the microstructure and its influence on the steel's performance during engineering applications.

Fatigue properties of bainitic steels have been broadly studied.<sup>[13,16–21]</sup> It is suggested that the propagation of fatigue crack is strongly influenced by microstructural barriers such as, bainite block boundaries, packet boundaries, and prior austenite grain boundaries.<sup>[16–18]</sup> It was reported that carbides in CBB may reduce the fatigue life by causing stress concentration during cyclic loading.<sup>[19]</sup> However, the impact of RA in CFB is relatively complicated. It is reported that RA may transform to martensite at the crack tip, which absorbs the energy required for crack propagation and decelerates the crack growth. On the other hand, Gao et al.<sup>[13]</sup> showed that while interplate film-like RA arrested the crack growth via martensitic transformation and changed the active slip system, the blocky RA or MA islands located at prior austenite grain boundaries led to intergranular fatigue cracking. However, most of the studies focused on the fatigue behavior of CFB and there are only a limited number of comparative studies on CBB and CFB in high-cycle fatigue (HCF) regimes.

The fatigue limit is one of the most important measures for engineering applications and outcome of a fatigue test series. It essentially quantifies the stress amplitude limit below which macroscopic fatigue crack should not initiate during cyclic loading, which is used to design components to avoid failures and promote sustainability. As one of the traditional methods, staircase test method (up-and-down method) is often used to determine the fatigue limit of materials.<sup>[22–25]</sup> Although determination of fatigue limit via traditional methods might be more reliable, it is still expensive, time-consuming, and requires a large amount of specimens.<sup>[26,27]</sup> In recent years, multiple studies are conducted for rapid determination of fatigue limit (or fatigue life) based on temperature evolution of specimens during fatigue testing correlated with fatigue damage of material, which is used to estimate the fatigue strength and the fatigue limit.<sup>[26–33]</sup> It is important to develop efficient, cheaper, and compatible methods to estimate fatigue limit of materials, especially to increase the applicability of these tests for industrial purposes (e.g., component testing). The load increase test (LIT) is one of these methods being used to estimate fatigue limit of various materials,<sup>[31–33]</sup> which provides reliable estimation of fatigue limit in a time- and cost-efficient manner. However, most of the studies on

LIT are employed in low frequencies and relatively at small number of cycles.<sup>[31–33]</sup> For this matter, a new LIT procedure is proposed using a 1 kHz resonance fatigue testing machine to estimate fatigue limit of bainitic steels in HCF regimes.

The first aim of this study is the comprehensive characterization of microstructure, mechanical properties, and HCF behavior of CBB and CFB formed at two different temperatures. The second aim is the verification of the fatigue limit of the studied bainitic steels determined via staircase method with the results obtained from the proposed LIT.

## 2. Experimental Section

### 2.1. Materials

Two steel ingots (80 kg), Fe–0.2C–2.5Mn and Fe–0.2C–1.5Si–2.5Mn (wt%), were produced in a laboratory-scale vacuum induction furnace. The ingots of  $140 \times 140 \text{ mm}^2$  were homogenized at  $1200^\circ\text{C}$  and forged down to the billets of  $60 \times 60 \text{ mm}^2$ . Subsequently, another homogenization process for 5 h was performed followed by furnace cooling. Silicon was added to the second alloy to prevent cementite precipitation during the bainitic transformation. The measured chemical compositions of the two alloys were given in Table 1. Similarly, this chemical composition concept was chosen to generate CBB and CFB.

### 2.2. Dilatometry

Dilatometry was used to determine phase transformation temperatures ( $A_{c1}$ ,  $A_{c3}$ , and  $M_s$ ) as well as to characterize the transformation behavior during heat treatments. For the experiments, a DIL 805A/D (TA instruments, Germany) dilatometer and rectangular specimens ( $4.0 \times 7.0 \times 1.4 \text{ mm}^3$ ) were used. The  $A_{c1}$  and  $A_{c3}$  were determined using a heating rate of  $0.05 \text{ K s}^{-1}$ . The  $M_s$  was determined via quenching the specimens to room temperature with a cooling rate of  $100 \text{ K s}^{-1}$  after the austenitization was completed, which was determined to be  $\approx M_s = 375^\circ\text{C}$  for both alloys. For the rest of the experiments, the heating rate was set to  $3.33 \text{ K s}^{-1}$ , where as the austenitization temperature was selected as  $A_{c3} + 60 \text{ K}$  for a duration of 300 s for both steels to ensure fully austenitic microstructures. With respect to the isothermal heat treatments, the specimens were cooled with  $100 \text{ K s}^{-1}$  to isothermal holding temperatures of 400 and  $450^\circ\text{C}$  and held for 45 min, respectively. This was followed by a final quenching to room temperature with  $100 \text{ K s}^{-1}$ . The dilatometer experiments were graphically represented, and the material annotations based on the alloy and heat

**Table 1.** Chemical compositions of the investigated steels in wt.-%. The chemical compositions were determined with optical emission spectroscopy (OES) and carbon was determined with combustion analysis.

Alloy	C	Si	Mn	P	S	Cr	Mo	Al	Cu
CBB	0.18	0.01	2.48	0.003	0.002	0.04	0.01	0.002	0.02
CFB	0.19	1.48	2.38	0.003	0.003	0.04	0.01	0.003	0.02

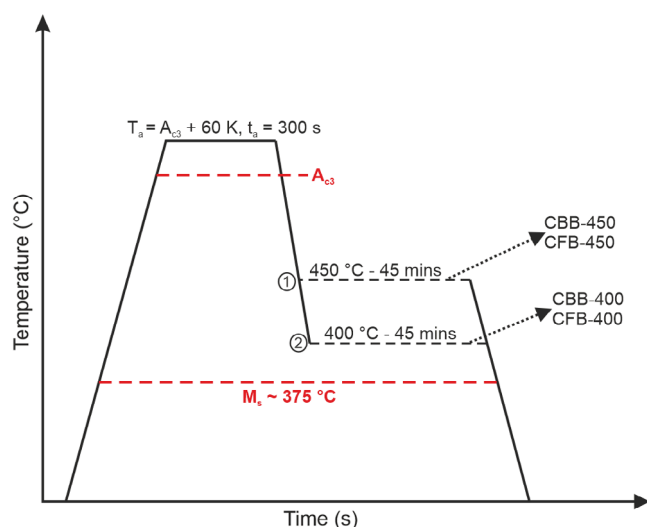


**Figure 1.** Schematic time–temperature diagram of dilatometer experiments for CBB and CFB alloys.

treatments were shown in **Figure 1**. To investigate the mechanical and fatigue properties of the materials, heat treatments were reproduced in salt baths for the testing samples.

### 2.3. Microstructural Investigation

The surface of the specimens was prepared for metallographic analysis by mechanical grinding up to 1200 SiC grit paper followed by polishing with 6 and 1  $\mu\text{m}$  diamond paste. Subsequently, the specimens were etched with 3%  $\text{HNO}_3$  (Nital). Scanning electron microscopy (SEM) investigations were carried out using a field-emission gun Zeiss Sigma SEM (Carl Zeiss Microscopy GmbH, Germany) with a 30  $\mu\text{m}$  aperture, an accelerating voltage of 15 kV and a working distance of 9 mm for the secondary electron (SE) detector, where as the accelerating voltage and working distance were reduced to 5 kV and 2 mm, respectively, for the high-resolution measurements with InLens detector. For the fracture surface investigations of the fatigue specimens, the SEM was employed with aperture sizes up to 75  $\mu\text{m}$ , an accelerating voltage of 15 kV, and working distances up to 20 mm using the SE detector. For electron backscatter diffraction (EBSD) measurements, the specimens were polished with oxide polishing suspension (OPS) for  $\approx 20$  min after the final mechanical polishing step. The EBSD measurements were conducted using a NordlysNano (Oxford Instruments, Great Britain) detector with a 75  $\mu\text{m}$  aperture, an accelerating voltage of 20 kV, a working distance of 17 mm, and a step size of 100 nm for the CBB alloys, where as it was reduced to 50 nm for the CFB alloys to be able to detect nanoscale RA. The SEM images were analyzed with ImageJ software to determine the width of BF plates and RA films of the CFB alloys. Postprocessing of the EBSD data was carried out with the MATLAB (MathWorks Inc., USA) toolbox MTEX.<sup>[34]</sup> Low-angle grain boundaries were defined by a misorientation angle  $5^\circ \leq \theta \leq 15^\circ$ , where as high-angle grain boundaries were defined as  $\theta > 15^\circ$ .

For the carbide analysis, a customized MATLAB script for rule-based image processing was written based on ref. [35,36] Grain boundaries with similar pixel values as the carbides were filtered by first applying a low circularity value to MATLAB's regionprops function using Image Processing Toolbox and subsequently subtracting the filtered grain boundary regions from the mask. Finally, the total carbide fraction, carbide area, and carbide equivalent diameter were calculated from the final mask. In total, three micrographs were analyzed covering  $57 \times 53 \mu\text{m}^2$  per image and averaged for each CBB material condition.

A deep learning model was used as a second approach to segment the MA islands in CFB steel. The model was previously trained on SEM micrographs of bainitic steels with  $512 \times 512$  image size. For further details on the training data, used model, and hyperparameters, the reader was referred to ref. [37] The calculation of the MA fraction per image was based on 48 cropped images to  $512 \times 512$  px covering a total area of  $170 \times 228 \mu\text{m}^2$ .

### 2.4. Retained Austenite Measurement

To quantify and compare the RA phase fractions of the CFB alloys, EBSD, Feritscope, and synchrotron X-ray diffraction (SYXRD) were employed. Details for the EBSD measurements and postprocessing were explained in Section 2.3. Ferromagnetic portion of the CFB alloys was determined via Feritscope (Helmut Fischer GmbH, Germany) to obtain RA fraction. Calibration of the Feritscope was done using standard magnetic saturation via 14.7%, 30.6%, 86.2%, and 100% ferromagnetic materials supplied by the manufacturer. For each specimen, the RA phase fraction was computed as an average of ten measurements. Ex situ SYXRD experiments were conducted at beamline P21.1 of PETRA III at Deutsches Elektronen-Synchrotron Center (DESY) in Hamburg, Germany. The beamline was operated at a fixed energy of 82.5 kV, supplying X-ray with a wavelength of  $\approx 0.15 \text{ \AA}$ . Postprocessing of the obtained diffraction profiles to quantify the RA fractions of CFB alloys was done via Rietveld refinement method with Materials Analysis Using Diffraction (MAUD) software.<sup>[38]</sup>

### 2.5. Mechanical Testing

For uniaxial tensile tests, B5  $\times$  25 cylindrical tensile specimens with a gauge diameter of 5 mm and a gauge length of 25 mm were used. The uniaxial tensile tests were performed with a universal electromechanical testing machine ZWICKROELL Z100 (ZwickRoell GmbH & Co. KG, Germany) at room temperature with a strain rate of  $0.001 \text{ s}^{-1}$ . Three tensile specimens were tested for each condition. After the completion of the tensile tests, one tensile specimen from each CFB alloy was sectioned  $\approx 10$  mm below the fracture surface for microstructural characterization. The preparation of the sectioned surfaces was done according to Section 2.3. Moreover, hardness of the dilatometer specimens was measured using Vickers 10 (HV10) indentation. To make sure that the hardness values were representative, five indentations were done on different positions of the specimens and the average of these measurements was taken as a representative hardness value of the materials.

## 2.6. Fatigue Testing

For fatigue tests, cylindrical fatigue specimens with the smallest gauge diameter of 4 mm and a total length of 107 mm were used. The surface of the specimens was mechanically polished with diamond paste down to 1  $\mu\text{m}$  to increase the surface quality. The tests were performed on a RUMUL GIGAFORE 50 (Russenberger Prüfmachinen AG, Switzerland) resonant testing machine with a testing frequency of 1 kHz and a stress ratio of  $R = -1$ .

For LIT, only one specimen was used for each material state. Tests were started from an initial stress amplitude and tested for  $10^6$  cycles. After each  $10^6$  cycles, the test was stopped and the stress amplitude was increased by 10 MPa. This procedure was applied until the fracture occurred. The temperature of the specimen surface was monitored via a thermocouple during the tests and cooling was not applied.

For staircase testing, 8–10 specimens were used for each material state. The test limit was set to  $10^7$  cycles. With respect to this, specimens that failed before the test limit were annotated as failures, whereas the ones that survived  $10^7$  cycles were annotated as runouts. In the case of a failure or a runout, the stress amplitude was respectively decreased or increased by 5 MPa in the subsequent test. The specimens were cooled down via air cooling during the tests. Moreover, the average fatigue limit derived from the staircase method was determined by the equation from Dixon–Mood.<sup>[23]</sup> The equation for the average fatigue limit is

$$\mu = S_0 + \Delta S \left( \frac{\sum_{i=0}^{i_{\max}} i n_i}{\sum_{i=0}^{i_{\max}} n_i} \mp 0.5 \right) \quad (1)$$

where  $S_0$  is the minimum stress amplitude of the less frequent occurrence of failed or survived specimens,  $\Delta S$  is the step size, the parameter  $i$  is an integer which represents the stress amplitude level,  $i_{\max}$  is the highest stress amplitude level reached in staircase,  $n_i$  is the number of specimens of the less frequent event at stress amplitude level  $i$ . If the failure is more frequent,  $i = 0$  corresponds to the lowest stress amplitude level at which a specimen survives. On the contrary, if the survival is more frequent,  $i = 0$  is the lowest stress amplitude level at which specimen fails. The plus sign (+) in Equation (1) is used when failure is more frequent, whereas the minus sign (–) is used when survival is more frequent. In the case of an equal number of

failures and survivals, the same result would be expected as a result of both calculations.

## 3. Results

### 3.1. Dilatometry

Dilatometer specimens of both steels were isothermally heat treated at 400 and 450 °C as represented in Figure 1. After austenitization, the specimens were first quenched to isothermal holding temperatures, which appeared as a sudden increase in dilatation curves (Figure 2b,c). After isothermal holding, the specimens were subsequently quenched down to room temperature. In Figure 2a, the relative length change as a function of time during isothermal holding is displayed. It can be seen that, after sufficient time, all curves reached a plateau, which indicates that bainitic transformation was completed in all states. The relative change in length, after the bainitic phase transformation was completed, increased with decreasing isothermal holding temperature in both steels. In CBB alloy, it rose from 0.55% to 0.59% with a decrease of isothermal holding temperature from 450 to 400 °C, respectively. A similar trend was observed in CFB alloy by an increment from 0.41% to 0.51% with a decrease of temperature from 450 to 400 °C, respectively.

Dilatation curves of each heat treatment state after austenitization are shown in Figure 2b,c. There was no trace of further phase transformation during subsequent cooling in CBB-400 and CBB-450, indicated by no deflection in the dilatation curves (Figure 2b). This was also the case for the CFB-400 (Figure 2c). On the other hand, such a deflection was observed in the dilatation curve of CFB-450 around 100 °C (as highlighted in Figure 2c), which suggests a martensitic transformation during subsequent cooling after bainitic transformation at 450 °C.

### 3.2. Microstructure

SEM images of CBB-400 and CBB-450 are shown in Figure 3a,b, respectively. It was revealed that in both states, BF was formed as matrix and excessive carbon was precipitated as cementite, as intended. The cementite precipitates were distributed in the BF with a certain direction ( $\approx 60^\circ$  with respect to the growth direction of BF) during bainitic phase transformation. SEM

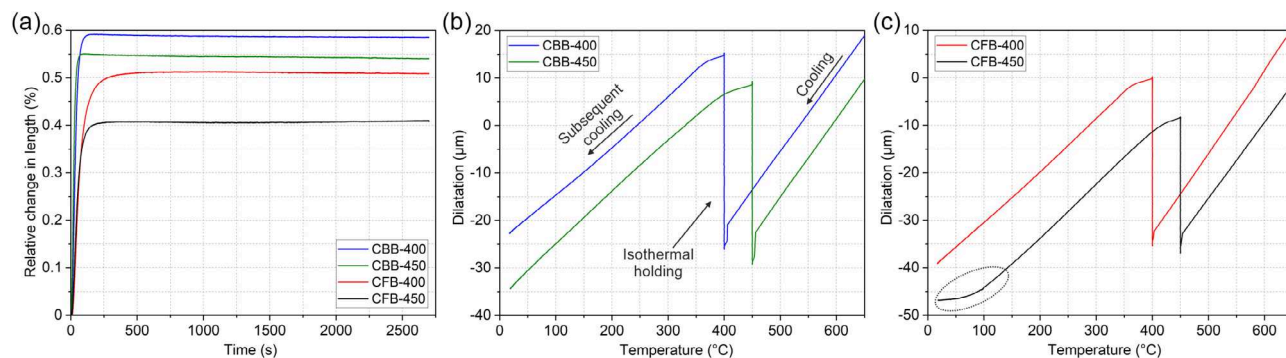


**Figure 2.** a) Relative length change as a function of time during isothermal holding, b) dilatation curves of CBB-400 and 450, and c) dilatation curves of CFB-400 and 450.



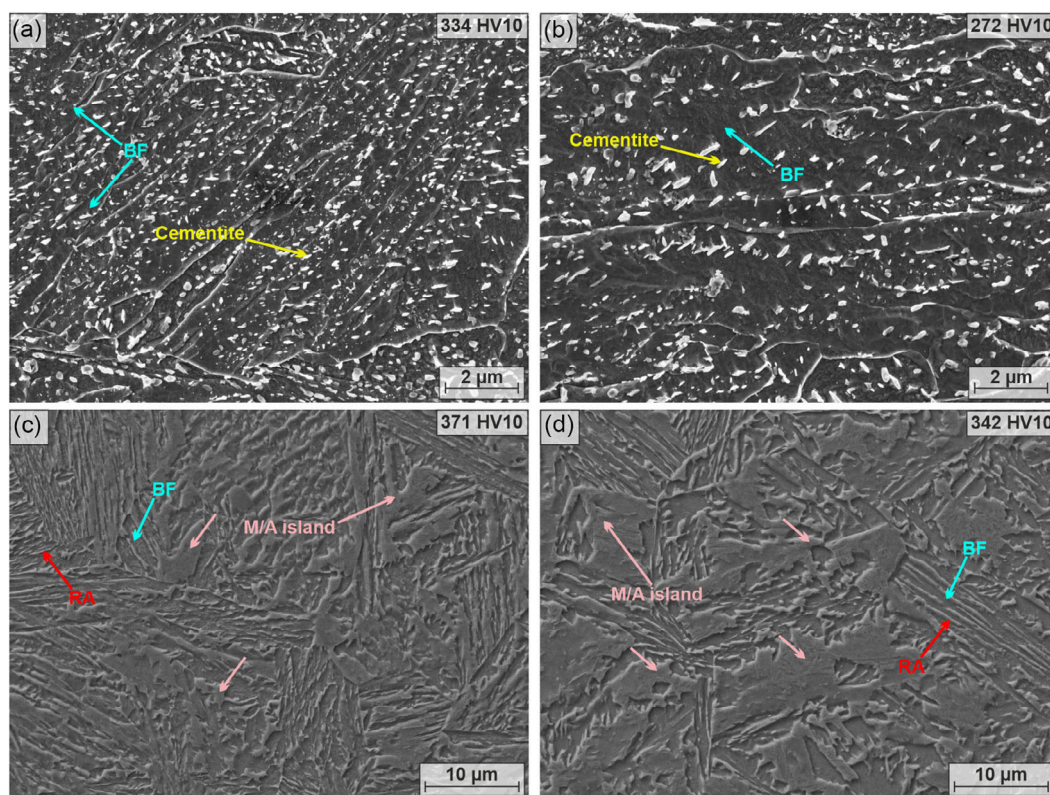


**Figure 3.** SEM images of a) CBB-400 and b) CBB-450 acquired via InLens detector, c) CFB-400 and d) CFB-450 acquired via SE detector.

**Table 2.** Average carbide diameter, average area of a carbide, and average carbide fraction with standard deviations based on analysis done on a surface area of three micrographs covering in total of  $\approx 7282 \mu\text{m}^2$ .

Material state	Carbide diameter [nm]	Carbide area [ $\times 10^5 \text{ nm}^2$ ]	Carbide fraction [%]
CBB-400	$321.73 \pm 5.75$	$1.10 \pm 0.04$	$13.38 \pm 0.36$
CBB-450	$350.17 \pm 13.32$	$1.35 \pm 0.12$	$9.94 \pm 0.85$

images revealed a coarser cementite morphology with an increase in isothermal holding temperature in CBB-450, where as cementite particles were finely dispersed in CBB-400. Statistical results obtained from quantitative carbide analysis on a surface area of CBB alloys, as displayed in **Table 2**, were in a good agreement with the qualitative observation of the SEM images. Carbide diameter increased from 321 to 350 nm, the average area of a single carbide increased from  $1.1 \times 10^5$  to  $1.35 \times 10^5 \text{ nm}^2$ , where as carbide fraction decreased from 13.4% to 10% with an increase of transformation temperature from 400 to 450 °C. In addition, there was no trace of martensite or MA islands in the microstructure of both states, which is an indication of no RA in the microstructure. This was also supported by the EBSD phase maps, shown in **Figure 4a,b**, where no RA was indexed both in CBB-400 and CBB-450.

CFB-400 and CFB-450 exhibited plate-like BF as displayed in **Figure 3c,d**, respectively. The RA films were observed in between the BF plates. It was noticed that the microstructure became finer

with decreasing isothermal holding temperature. The average width of the BF plates was measured as  $0.15 \mu\text{m}$  in CFB-400, where as it was increased to  $0.24 \mu\text{m}$  in CFB-450. Similarly, the average width of the film-like RA was  $0.16 \mu\text{m}$  in CFB-400, where as it went up to  $0.30 \mu\text{m}$  in CFB-450. The summary of BF and RA width of CFB alloys can be found in **Table 3**.

In addition, MA islands were observed in both states of CFB alloy (**Figure 3c,d**). The amount and size of the MA islands decreased with decreasing isothermal holding temperature in CFB-400. **Table 4** shows the amount of segmented MA islands via deep learning evaluation model as well as unindexed pixels obtained during EBSD measurements for CFB alloys. Regarding the deep learning model, the fraction of MA islands was determined as 17.9% in CFB-450, where as it was decreased to 11.7% in CFB-400. When EBSD phase maps of CFB alloys are considered, the fraction of unindexed pixels (displayed in orange) was considerably high (**Figure 4c,d**). The fraction of the unindexed pixels was 8.8% in CFB-400, where as it was increased to 19% in the CFB-450. It is worth to mention that the fraction of unindexed pixels obtained for CFB-alloys was in good agreement with the MA island fractions acquired via segmentation model (**Table 4**). On top of this, most of the unindexed pixels appeared as big clusters consisting of very small RA particles (**Figure 4c,d**). Moreover, the size and morphology of these big unindexed clusters displayed substantial similarities with the MA islands observed in **Figure 3c,d**.

Based on the EBSD phase maps, not only film-like RA but also blocky type RA was detected, especially in CFB-400 (**Figure 4c**).

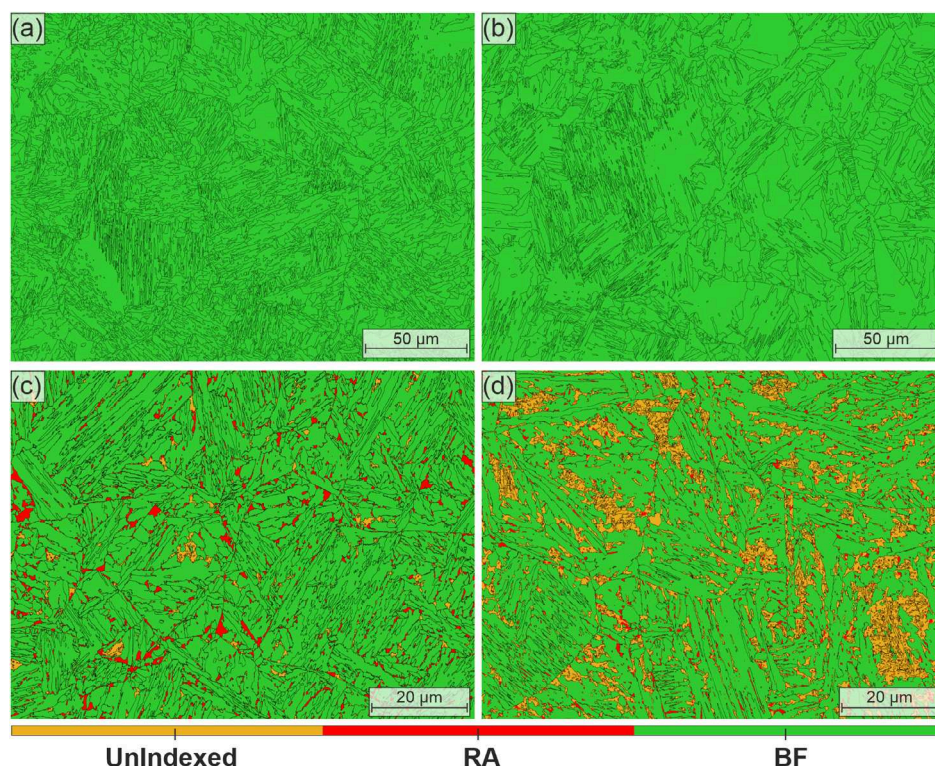


**Figure 4.** EBSD phase maps of a) CBB-400, b) CBB-450, c) CFB-400, and d) CFB-450.

**Table 3.** Average width of BF plates and RA films of CFB-400 and CFB-450.

Material state	Bainitic ferrite [ $\mu\text{m}$ ]	Retained austenite [ $\mu\text{m}$ ]
CFB-400	$0.15 \pm 0.04$	$0.16 \pm 0.05$
CFB-450	$0.24 \pm 0.06$	$0.30 \pm 0.07$

**Table 4.** Fraction of segmented MA islands and unindexed pixels in EBSD maps of CFB alloys.

Material state	Segmented MA islands [%]	EBSD unindexed pixels [%]
CFB-400	$11.7 \pm 3.3$	8.8
CFB-450	$17.9 \pm 4.2$	19

It was recognized that the blocky RA was mostly located on the prior austenite grains boundaries (PAGB). In the case of CFB-450, instead of blocky RA, mostly big unindexed clusters were observed located on the PAGB, where as small RA particles were indexed in or around these clusters (Figure 4d).

Moreover, the CFB-400 exhibited 3.3% RA, where as it was 1.1% in CFB-450 (displayed in red) according to the EBSD measurements. However, RA detected via EBSD was significantly lower compared to the results acquired via Feritscope and Synchrotron X-ray diffraction (SYXRD). In CFB-400, the fraction of RA measured as 16.2% and 14.3%, where as it was 8.9% and 8.7% in CFB-450 via Feritscope and SYXRD, respectively. The RA measurements via different techniques are shown in

**Table 5.** Retained austenite fraction of CFB alloys obtained via different methods.

Material state	EBSD [%]	Feritscope [%]	SYXRD [%]
CFB-400	3.3	$16.2 \pm 0.6$	14.3
CFB-450	1.1	$8.9 \pm 0.5$	8.7

**Table 5.** Overall results showed that the CFB-400 contained more RA in the final microstructure compared to CFB-450.

### 3.3. Mechanical Properties

**Table 6** shows the mechanical properties for each specimen condition. Furthermore, engineering stress–strain curves are presented in **Figure 5a**. Similar in **Figure 5a**, all stress–strain curves exhibited continuous yielding behavior and uniform plastic deformation. The CFB alloys exhibited considerably better

**Table 6.** Mechanical properties of the materials.

Material state	$R_{p0.2}$ [MPa]	$R_m$ [MPa]	$A_g$ [%]	$A_5$ [%]	Hardness [HV10]
CBB-400	$738 \pm 13$	$866 \pm 12$	$4.2 \pm 0.7$	$13.4 \pm 0.6$	$334 \pm 7$
CBB-450	$589 \pm 13$	$720 \pm 17$	$6.0 \pm 0.9$	$16.8 \pm 1.2$	$272 \pm 9$
CFB-400	$765 \pm 5$	$1134 \pm 4$	$11.6 \pm 0.6$	$19.4 \pm 0.2$	$371 \pm 5$
CFB-450	$667 \pm 5$	$1137 \pm 15$	$8.5 \pm 1.0$	$14.3 \pm 2.0$	$342 \pm 3$



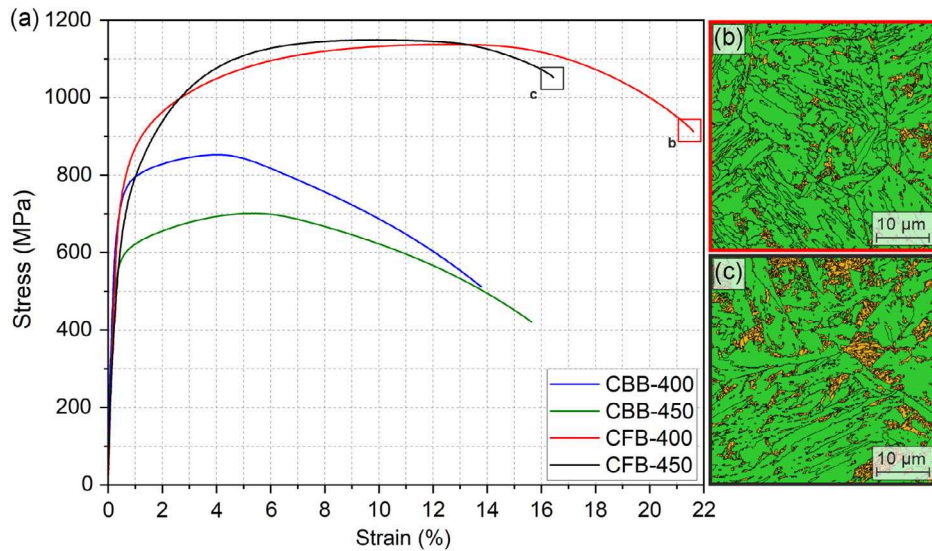


**Figure 5.** a) Engineering stress–strain curves of all CBB and CFB alloys. EBSD phase map of b) CFB-400 and c) CFB-450 after deformation.

mechanical properties than the CBB alloys, that is, higher strength, ductility, as well as hardness.

In the CBB alloy, with the holding temperature decreasing from 450 to 400 °C, the yield strength ( $R_{p0.2}$ ) increased from 589 to 738 MPa, the tensile strength ( $R_m$ ) increased from 720 to 866 MPa and the hardness increased from 272 to 334 HV10. In contrast, the uniform elongation ( $A_g$ ) decreased from 6.0% to 4.2%, where as the total elongation ( $A_5$ ) decreased from 16.8% to 13.4%.

In the case of the CFB alloy, a similar trend was noticed on the change of the mechanical properties, when the isothermal holding temperature was decreased from 450 to 400 °C. The yield strength increased from 667 to 765 MPa, the hardness increased from 342 to 371 HV10, where as the tensile strength of both specimens remained between 1130 and 1140 MPa. The uniform elongation was raised from 8.5% to 11.6%, where as the total elongation was raised from 14.3% to 19.4%. Apart from that, EBSD phase maps of CFB-400 and CFB-450 are shown in Figure 5b,c, respectively. Unlike the undeformed state of CFB alloys (Figure 4c,d), only traces of RA were found after deformation.

### 3.4. Fatigue Properties

LIT was conducted for each material state (Figure 6a,c,e,g). For the CBB alloys, the initial stress amplitude was set to 300 MPa, where as it was set to 400 MPa for CFB alloys, values being far below the yield strength of the materials (see Table 6). After each  $10^6$  cycles, the test was stopped and the stress amplitude was increased by 10 MPa until the fracture occurred. The temperature of the specimen surface was monitored via a thermocouple during the tests. It was observed that the temperature increased with increasing number of cycles and stress amplitude in all specimens. Before the specimens failed, the temperature increase became significant compared to the main phase of the test. Moreover, the stress amplitude, where the significant temperature jump occurred, was presumed as an approximation of the fatigue limit of the material. In general, it is clear that the

CFB alloys exhibited substantially better performance during LIT. For CBB-400 and CBB-450, both specimens failed when the stress amplitude reached to 340 MPa (Figure 6a,c). In the case of CFB-400 and CFB-450, the specimens failed at a stress amplitude of 470 and 450 MPa, respectively (Figure 6e,g). It is also worth mentioning that the temperatures reached in CFB alloys were considerably higher than what was achieved in CBB alloys.

In addition, and to verify the LIT, the staircase method was applied to determine the fatigue limit of the materials. The test limit was set to  $10^7$  cycles. If a specimen failed at cycles less than  $10^7$ , the stress amplitude was decreased by 5 MPa for the next test. Otherwise, the stress amplitude was increased by 5 MPa for the subsequent test. Average fatigue limit values of each material were calculated by the Dixon–Mood equations.<sup>[23]</sup> Graphical representations of staircase testing results based on failures and survivals are given in Figure 6b,d,f,h for each material state. The average fatigue limit of CBB-400 was determined as 343 MPa, where as it decreased to 330 MPa in CBB-450. The CFB alloys exhibited a very higher fatigue limit by 495 and 479 MPa, respectively, in CFB-400 and CFB-450. Determined fatigue limit data of each material state via both methods are shown in Table 7.

In addition to the determination of the fatigue limit, fracture surface of the fatigue specimens were investigated via SEM to identify the fatigue crack origins of the investigated alloys. It was observed that the fatigue crack initiated from the surface (highlighted with black arrow) in all the materials (Appendix A, Figure A1, Supporting Information). Furthermore, the crack propagation region of CFB alloys were larger than the crack propagation region of CBB alloys. In all the failed specimens, including LIT, no other pattern was observed.

## 4. Discussion

### 4.1. The Effect of Heat Treatment on Microstructure

Microstructural investigations showed that silicon addition to CFB alloys prevented the cementite precipitation due to low

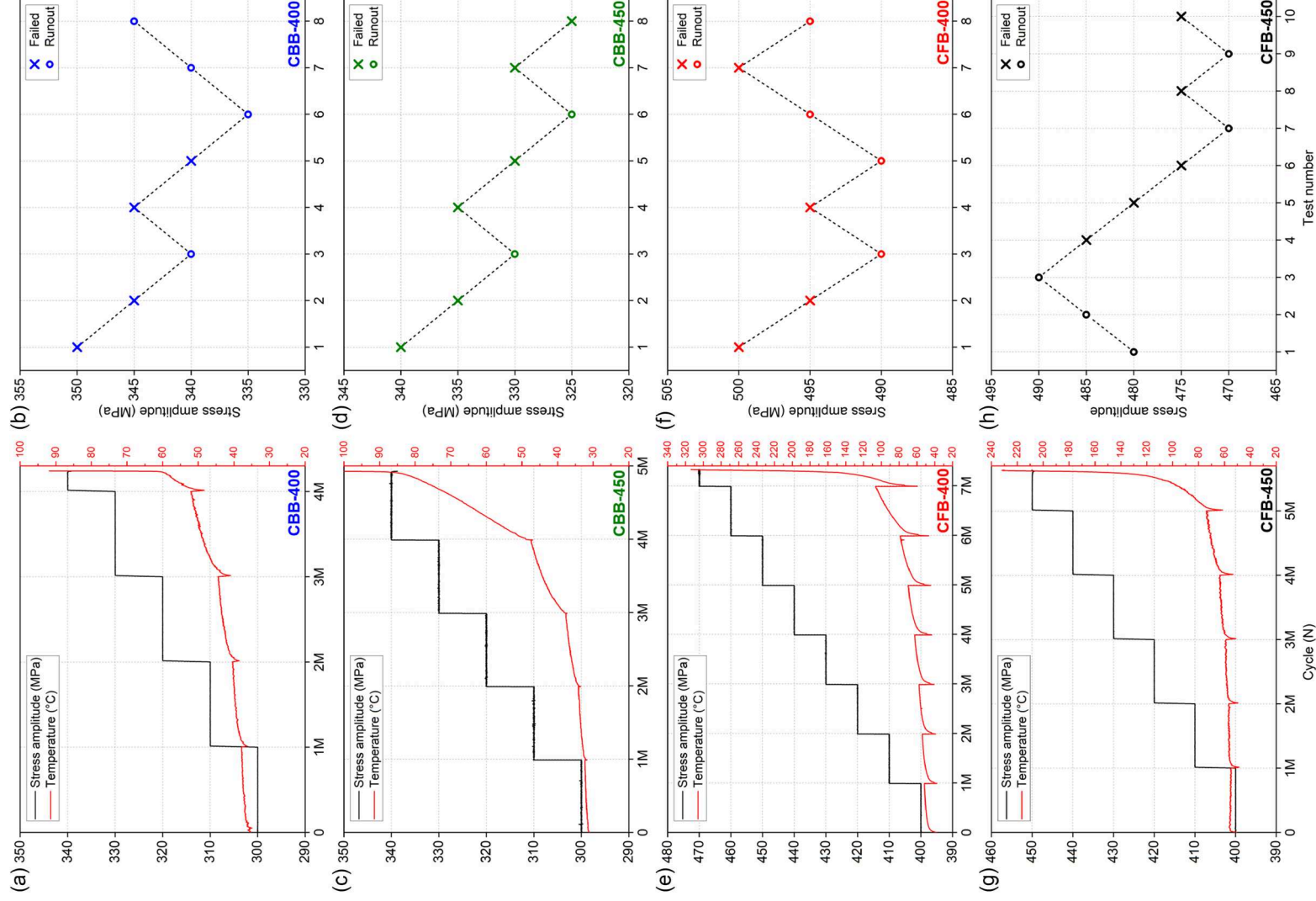




**Table 7.** Fatigue limit of the materials determined via load increase test and staircase method.

Material state	Fatigue limit determined by load increase test [MPa]	Fatigue limit determined by staircase method [MPa]
CBB-400	340	343
CBB-450	340	330
CFB-400	470	495
CFB-450	450	479

solubility of silicon in cementite.<sup>[6,7]</sup> Therefore, the excessive carbon, which was rejected from BF, was enriched into the surrounding austenite during the bainitic transformation, which resulted in thermal stabilization of austenite.<sup>[6,7]</sup> Therefore, RA was observed in CFB alloys at room temperature, where as cementite precipitates were observed in CBB alloys (Figure 3).

In CBB-400, cementite precipitates showed a finer morphology and a denser distribution compared to the ones in CBB-450 (Figure 3a,b). Because of slower kinetics as a result of lower isothermal transformation temperature of CBB-400, time required for carbide precipitation increases. Therefore, it is possible that some of the carbon was trapped and/or precipitated as carbides in the BF, where as the rest was partitioned in surrounding austenite and/or precipitated as cementite.<sup>[2,39]</sup> Highly magnified InLens micrographs of CBB-400, shown in Figure 7a, also underpinned this hypothesis by depicting very small precipitates, which points to carbide precipitation in the BF. Contrary to this, although some smaller precipitates were visible in the micrograph of CBB-450 (Figure 7d), it was negligible compared to CBB-400. For the same reason, cementite between the BF was refined since only a part of the carbon had the opportunity to be partitioned into austenite and precipitated.

The results revealed that the inefficient detection of RA via EBSD compared to Feritscope and SYXRD. Using EBSD, only a small surface area of the specimen can be investigated. In contrast, Feritscope and SYXRD cover a certain volume of the specimens during the measurements. Another reason for insufficient RA identification is the nanoscale nature of RA films, which makes it harder to resolve them during EBSD measurement. When the phase maps of CFB-400 and CFB-450 are considered, most of the detected RA was in blocky morphology (Figure 4c,d). Similarly, the increased amount of martensitic constituents in the investigated area naturally decreases the amount of measured RA. Therefore, limited surface area and microstructural features of the investigated area may restrain the RA measurements via EBSD.

EBSD investigations of CFB alloys exhibited a considerable fraction of unindexed phases (Figure 4c,d), which can be attributed to the existence of MA islands in the microstructure. The fact that the unindexed regions appeared as big clusters as MA islands observed in SEM images (Figure 3c,d) and the size and fraction of these clusters were in good agreement with the MA islands in SEM images supported this attribution. Figure 7c,f show the band contrast (BC) maps combined with austenite phase maps for CFB-400 and CFB-450, respectively. The unindexed regions observed on the phase maps coincide with dark areas on the BC maps. It is highly likely that MA islands were not indexed because of low Kikuchi pattern quality due to high-defect density of martensitic constituents and appeared as dark on the BC maps. In addition, especially in the large unindexed regions of CFB-450, small RA particles were indexed, demonstrating the presence of untransformed RA in these regions (Figure 4d), which provides an argument for the presence of MA islands.<sup>[40]</sup> Besides this, it is significant to note that the CBB alloys, containing no martensite, displayed negligible fraction of unindexed phases compared to martensite containing

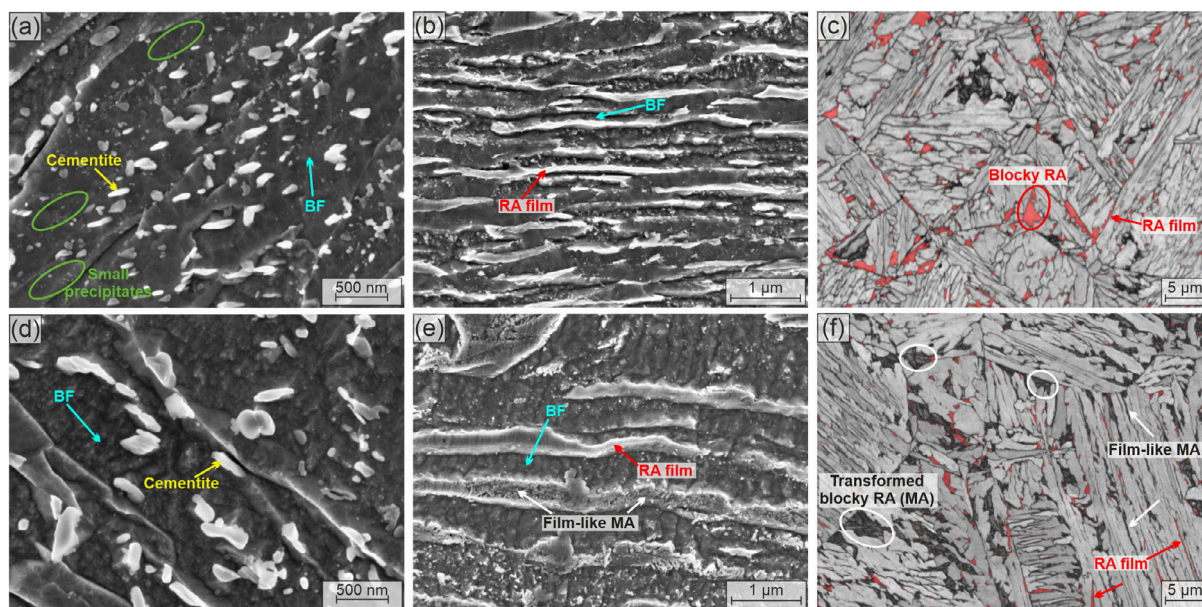


**Figure 7.** SEM images acquired via InLens detector of a) CBB-400, d) CBB-450, b) CFB-400, and e) CFB-450. BC map combined with austenite phase of c) CFB-400 and f) CFB-450.

CFB alloys. As a result, unindexed regions in the EBSD phase maps of CFB alloys were considered as MA islands.

The amount and size of MA islands decreased with decreasing transformation temperature. This can be related to the influence of bainite transformation temperature on BF fraction, carbon partitioning, and correspondingly, on the morphology and stability of the RA after the transformation is completed. It is widely accepted that there are two main types of austenite in CFB microstructures. One of them is nanoscale film-like austenite formed in between BF plates, the other one is rather extensive and blocky austenite.<sup>[4]</sup> According to incomplete-reaction phenomenon ( $T_0$  concept),<sup>[14]</sup> with decreasing isothermal phase transformation temperature the diffusionless transformation of bainite can proceed even further until a critical carbon concentration is reached, where the free energy of BF is no longer less than that of austenite. Here in, at higher transformation temperatures, due to less BF formation and carbon partitioning, more blocky austenite will remain in the microstructure with less carbon enrichment, which would lead to martensitic transformation during subsequent cooling.<sup>[8]</sup> Although blocky RA on the PAGB was visible in CFB-400 (Figure 7c), multiple large dark clusters on PAGB with a similar morphology were realized in CFB-450 (Figure 7f) indicating MA island formation due to lower stability of RA in CFB-450. The dilatation curve obtained for CFB-450 supported this observation by showing a pronounced martensitic transformation during subsequent cooling (Figure 2c), which indicates the higher  $M_s$  associated with the blocky RA due to lower thermal stability.

It was also observed that the width of BF plates and RA films decreased with decreasing transformation temperature, which is in good agreement with the literature.<sup>[15,41–43]</sup> After a BF plate forms, a carbon-enriched zone forms around the BF plate due to carbon partitioning, and carbon concentration of this zone drops by distance.<sup>[44]</sup> Regarding the  $T_0$  concept, spontaneous transformation of austenite to BF can only occur when the carbon concentration in austenite is below a certain level. In addition, at lower transformation temperatures, BF formation can start at higher carbon concentrations at the austenite interface compared to higher transformation temperatures.<sup>[14]</sup> Therefore, at 400 °C, the next BF plate can thermodynamically start forming from a smaller distance compared to 450 °C, which was inherited as thinner RA films in the microstructure of CFB-400.<sup>[44]</sup> In addition, the reduction in the BF plate width in CFB-400 can be explained by increasing strength of the RA with decreasing transformation temperature.<sup>[45]</sup> It was established that the shape change due to diffusionless bainite transformation is not accommodated elastically. In contrast, plastic relaxation is observed in the austenite adjacent to BF plate, which creates a dislocation debris that resists the further growth of BF plate. Therefore, the mechanically stronger the RA, the greater the resistance against the advancement of BF interface.<sup>[45]</sup>

Although the RA fraction of CFB-450 should have been higher considering the  $T_0$  concept, CFB-400 exhibited a higher RA fraction in the final microstructure (Table 5). The reason might be the influence of morphology, size, and stability of RA explained above. Figure 7b,e display the images acquired via InLens detector for CFB-400 and CFB-450, respectively. These images also confirmed the low-thermal stability of RA in CFB-450, for which some of the RA films were already partly transformed to

martensite (highlighted with white arrow in Figure 7e) during subsequent cooling after isothermal treatment at 450 °C, inherited by highly deformed appearance in the micrograph. This was also reflected in Figure 7f by coexistence of film-like RA (highlighted with red arrow) and dark film-like morphologies (highlighted with white arrow). In contrast, this was not the case for CFB-400 as shown in Figure 7b,c, which indicates the higher stability of the RA in CFB-400. Therefore, it is highly possible that not only the blocky RA but also some of the film-like RA transformed partly to martensite due to low-thermal stability, which led to low detection of RA as well as increased amount of film-like unindexed regions in the EBSD measurements of CFB-450.

## 4.2. Mechanical Properties

As a general comparison, CFB alloys clearly exhibited better mechanical properties, which is related to the microstructural differences. CFB alloys displayed significantly higher strength as well as higher uniform and total elongation than CBB alloys. The face-centered cubic RA phase can facilitate more dislocation motion than the face-centered cubic phase, which enhances the plasticity of the material during deformation.<sup>[19]</sup> In addition, the elongation can be enhanced with the introduction of RA into the bainitic microstructure, which can be altered by the processing parameters.<sup>[15]</sup> Furthermore, the metastable RA transformed to martensite progressively through TRIP effect during plastic deformation, which was indicated by the absence of RA in the microstructure after deformation (Figure 5b,c). This may lead to better deformability as well as higher tensile strength and hardness.<sup>[10,46]</sup> Moreover, solid solution strengthening due to silicon alloying is another factor that improved the mechanical properties of CFB alloys.<sup>[19,41,47]</sup>

Decreased phase transformation temperature enhanced the mechanical properties of CBB alloys. The finer carbide distribution associated with finer BF in the microstructure clearly increased the hardness, yield strength, and tensile strength of CBB-400. It is worth mentioning that this substantial improvement was not accompanied by a significant loss in ductility. Moreover, when the area below the stress–strain curve of CBB alloys is considered (Figure 5a), CBB-400 covered a larger area, which points out to higher toughness for CBB-400. Long et al.<sup>[41]</sup> also showed that the low-temperature CBB exhibited higher impact toughness than high-temperature CBB.

When the mechanical properties of the CFB alloys are considered, it is evident that mechanical properties became superior with decreasing phase transformation temperature as in CBB alloys. Increased yield strength and hardness of CFB-400 can be attributed to the increased fraction of stronger BF and refinement of the microstructure due to lower phase transformation temperature.<sup>[43]</sup> The martensitic constituents might have an influence on the increase of the yield strength and hardness of CFB-400. However, even though CFB-450 had a higher fraction of martensitic constituents, it exhibited lower yield strength and hardness. Therefore, the major reason behind this increase should be the BF fraction and refinement of the microstructure. In contrast, the tensile strength showed no improvement with a decrease in transformation temperature as in yield strength and



hardness. This indicates that the tensile strength has more dependency on the martensitic constituents existing both before and after deformation. When the microstructures are considered, CFB-400 consisted of more RA. However, if the microstructures prior to cooling just after the bainitic transformation are considered, CFB-450 is expected to have more austenite considering the  $T_0$  concept. A forementioned, some of the RA transformed to martensite during subsequent cooling due to low stability and the RA fraction in the final microstructure was reduced. This means that after deformation, the amount of martensite in the microstructure of CFB-450 should be more than CFB-400, which explains the compensation of tensile strength of CFB-450. Improved ductility of CFB-400 can be related to finely distributed film-like RA at higher fractions with higher stability. It was suggested that the best results were obtained when the RA was in the form of films between BF plates instead of big blocky morphology.<sup>[15]</sup> In addition, when the mechanical stability of RA increased to optimum levels, ductility can be improved by the enhanced elongation through prolonged TRIP effect.<sup>[11]</sup> Finally, as a side note, it was also shown that big blocky MA islands have a negative effect on the toughness properties due to unfavorable local stress concentrations and RA stability in the MA islands.<sup>[48]</sup>

### 4.3. Fatigue Properties

When the overall results obtained from LIT and staircase method considered, CFB alloys exhibited substantially higher fatigue limit than CBB alloys. It was shown that the fatigue limit and fatigue strength of metallic materials increases with increasing tensile strength until a critical value is reached.<sup>[49,50]</sup> Therefore, the higher fatigue limit of CFB alloys can be mainly attributed to the higher tensile strength. Superior fatigue properties of CFB alloys were also indicated by having larger crack propagation zone because of higher resistance to fatigue crack propagation, even at significantly higher stress amplitudes (Appendix A, Figure A1, Supporting Information). It was mentioned that carbides in CBB may form micropores during fatigue loading, increase the stress concentration, and decrease the fatigue life,<sup>[19]</sup> which could be another reason why CBB alloys displayed lower HCF performance overall. In addition, in the case of CFB, the metastable RA may transform to martensite due to TRIP effect induced by plastic deformation at the fatigue crack tip during crack propagation.<sup>[12,51]</sup> Huo et al.<sup>[52]</sup> demonstrated the interaction of fatigue crack propagation with RA. Because of the strain-induced transformation of RA to martensite, the system absorbs a significant amount of energy. It was stated that the fracture energy of martensite is smaller than the fracture energy of austenite, and the overall absorbed energy during the phase transformation from RA to martensite is bigger than the fracture energy difference of martensite and RA.<sup>[52–54]</sup> Thus, fatigue crack propagation can be decelerated and/or deflected (Appendix A, Figure A2, Supporting Information). Besides causing a volume expansion, the transformation of RA to martensite may result in the generation of compressive stresses at the fatigue crack tip. These compressive stresses can close the crack tip and it can only continue to propagate again when the compressive stress is eliminated.<sup>[12,52,55]</sup>

Comparing the HCF properties of CBB alloys, CBB-400 exhibited a slightly higher fatigue limit than CBB-450 (via staircase method). It was suggested that cementite plates could be strong barriers to crack growth during fatigue loading.<sup>[56,57]</sup> Therefore, finer distribution of cementite in CBB-400 could be linked to a greater fatigue limit among CBB alloys. In addition, as displayed in Figure 8a, the fraction of high-angle boundaries ( $>15^\circ$ ) increased in CBB-400, which are known to be effective barriers to fatigue cracks due to their highly misoriented nature.<sup>[54]</sup> It was calculated that 88% of the boundaries in CBB-450 were high-angle boundaries, as opposed to 93% in CBB-400. What is more interesting is that the relative frequency of the boundaries with a misorientation angle of  $55^\circ$  and greater was 70% in CBB-450, where as it was 79% in CBB-400. As a result of these factors, the fatigue cracks branch out in CBB-400. Therefore, the total path increases during crack propagation and more energy is required to reach to critical crack length and thus, the fatigue life is improved.<sup>[54]</sup>

Although the tensile strength of CFB alloys was very similar, fatigue limit of CFB-400 was prominently higher than that of

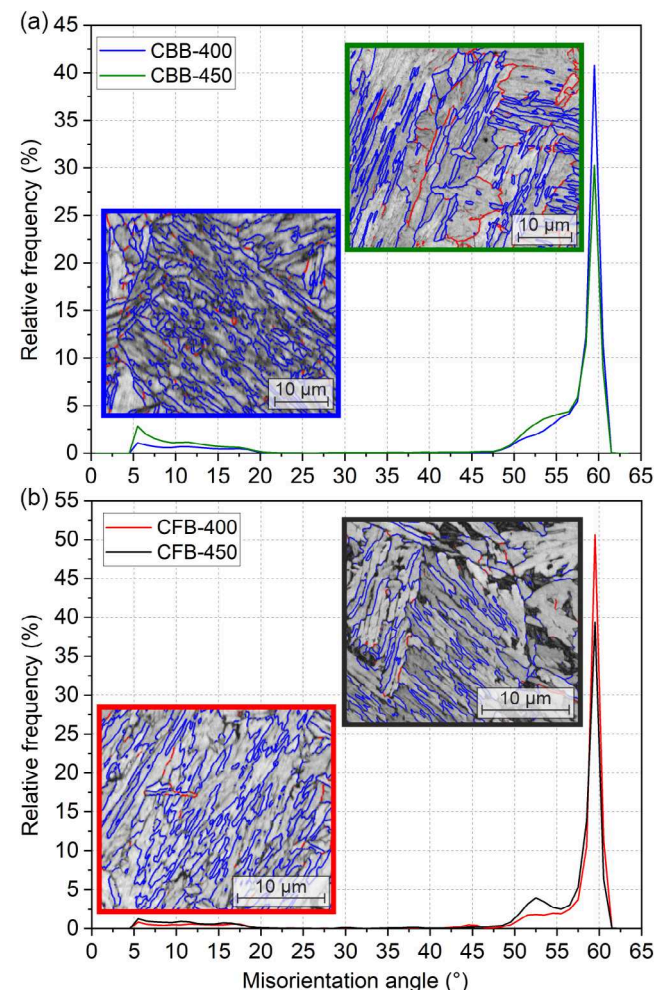


**Figure 8.** Grain boundary misorientation distribution of a) CBB and b) CFB alloys. Red- and blue-colored boundaries in the maps represent the low- and high-angle boundaries, respectively.



CFB-450. Enhanced fatigue limit of CFB-400 can be attributed to the following four reasons: 1) the increased number of effective barriers to prevent fatigue crack propagation due to finer morphology of BF plates and RA films; 2) with decreasing transformation temperature, fraction of the high-angle boundaries was also increased in CFB-400 (Figure 8b). The relative frequency of high-angle boundaries was 91% in CFB-450, which increased to 94% in CFB-400. In addition, 70% of the boundaries had misorientation angle of 55° and greater in CFB-450, where as this fraction was 81% in CFB 400. Compared to low-angle boundaries, high-angle boundaries are more effective barriers to deflect, decelerate, or even terminate the fatigue cracks;<sup>[54]</sup> 3) it is known that fraction, morphology, and stability of RA can be optimized via processing parameters to obtain better properties.<sup>[2,15]</sup> It is shown in the prior sections that the morphology and stability of the RA were positively altered in CFB-400, along with a higher fraction in the final microstructure compared to CFB-450. Owing to these modifications of RA, in the case of phase transformation from RA to martensite during fatigue crack propagation, more energy might be absorbed because of a prolonged TRIP effect; and 4) decreased amount and size of MA islands in the microstructure of CFB-400 might have favored the high-cycle properties. Gao et al.<sup>[13]</sup> showed that blocky RA or MA islands formed at prior austenite grain boundaries (PAGB) led to intergranular fatigue cracking due to slip impingement. Under normal circumstances, PAGB act as efficient microstructural barriers to prevent fatigue crack propagation.<sup>[16]</sup> However, as a result of blocky RA or MA island formation on the PAGB, the activation of the slip on the preferred plane of the RA becomes easier on the slip impingement, formed on the PAGB from adjacent PAG, leading to the intergranular fatigue crack.<sup>[13]</sup>

In addition to the HCF properties of the studied materials, comparison of two different methods to determine fatigue limit via high-frequency (1 kHz) resonance fatigue testing machine was conducted. Generally, it is possible to obtain more accurate results from the staircase method because it is based on a statistical approach with multiple test samples. Moreover, accuracy of the results can be improved via different parameters (e.g., step size) and more test samples. In contrast, as a consequence of the increased number of test samples, determination of fatigue limit becomes very expensive and time-consuming, even with 1 kHz testing equipment. It was observed that the results obtained from LIT were in good agreement with the results from staircase testing, especially for CBB alloys. In the case of CFB alloys, the determined fatigue limit via LIT was slightly lower than the fatigue limit determined via staircase method. When compared, significantly higher temperatures were reached in CFB alloys even in the initial stages of the LIT. At the end of the tests, CFB alloys reached temperatures beyond 200 °C, where as CBB alloys remained below 100 °C. The stress amplitudes applied to CFB alloys were also significantly higher compared to CBB alloys. Higher stress amplitudes in combination with high-testing frequencies is one of the reasons why higher temperatures were monitored in CFB alloys. In addition to the energy dissipation due to fatigue damage activities, martensitic transformation during cyclic loading might have caused an extra heat dissipation in CFB alloys, which was not the case for CBB alloys.

In the meantime, self-heating may influence the HCF properties.<sup>[58]</sup> Kozłowska et al.<sup>[59]</sup> displayed that during tensile testing, the intensity of strain-induced martensitic transformation of RA decreases because of higher stability of austenite that is corresponding to rise of stacking fault energy value of this phase.<sup>[59]</sup> Nikitin et al.<sup>[60]</sup> showed that temperature increase due self-heating inhibits the strain-induced martensitic transformation in austenitic stainless steels, which deteriorates the fatigue life. Furthermore, at high temperatures (200–300 °C), remaining RA and/or martensitic constituents may also decompose and affect the fatigue limit of the materials. Therefore, it is possible that higher temperatures due to anisothermal testing conditions may have influenced the obtained fatigue limit of CFB alloys. In contrast, the final temperature that was reached during the LIT has less importance regarding identifying the fatigue limit. If the temperature jump has already occurred, it means that the fatigue limit was already surpassed. Thus, the final temperature will have no influence on the fatigue limit as the fatigue limit is already exceeded.

However, the temperature during the LIT was still relatively high even before the final stress amplitude was reached, which may have an impact on the determined fatigue limit of CFB alloys. Therefore, some alterations in testing parameters can be made to obtain better results. For instance, active cooling can be used to observe the impact on the outcome of the test. The number of cycles to increase the stress amplitude and/or the step size of the stress amplitude increment can be changed to be able to identify the fatigue limit more accurately. Yet, it is important to consider that LIT is a one specimen test, which makes it substantially more time- and cost-efficient, and the empirical study revealed that it can provide an appropriate fatigue limit estimation of the studied materials.

## 5. Conclusions

In this work, a comprehensive study on CBB and CFB was performed. Assessment of HCF performance of the studied bainitic steels is completed and the influence of phase transformation temperature is investigated. A new LIT is proposed using a 1 kHz resonant testing machine as a rapid method to estimate the fatigue limit of studied bainitic steels in HCF regimes. The following conclusions can be drawn: 1) the proposed LIT is shown to be an efficient method to estimate the fatigue limit of the bainitic steels in HCF regimes as opposed to the time-consuming staircase method; 2) unindexed regions in the EBSD maps of CFB are successfully used to differentiate the MA islands. The obtained statistical data are instrumentally used to assess fatigue behavior of both alloys; 3) increased fraction and stability of RA with pronounced film-like morphology enhances the HCF performance of CFB by absorbing the energy required for crack propagation via improved TRIP effect, where as unstable blocky RA and/or MA islands formed at prior austenite grain boundaries are detrimental for HCF properties; and 4) finer carbide distribution and increased proportion of high-angle grain boundaries, as produced by lowering the transformation temperature of CBB, act as more effective barriers against fatigue crack propagation.

## Supporting Information

Supporting Information is available from the Wiley Online Library or from the author.

## Acknowledgements

This work was supported by the German Federal Ministry of Education and Research (BMBF) under grant numbers 13XP5118A, 13XP5118B and 13XP5118C. The authors acknowledge DESY (Hamburg, Germany), a member of the Helmholtz Association HGF, for the provision of experimental facilities. Parts of this research were carried out at PETRA III and the authors would like to thank Dr. Zoltan Hegedüs for assistance in using beamline P21.2. Beamtime was allocated for proposal I-20220679 EC. The help of Ahmet Turnali with SYXRD measurements is also gratefully acknowledged.

Open Access funding enabled and organized by Projekt DEAL.

## Conflict of Interest

The authors declare no conflict of interest.

## Data Availability Statement

The data that support the findings of this study are available from the corresponding author upon reasonable request.

## Keywords

bainite, EBSD, fatigues, microstructures, TRIP effect

Received: April 20, 2023

Revised: June 20, 2023

Published online:

- [1] A. Gramlich, W. Hagedorn, K. Greiff, U. Krupp, *Adv. Eng. Mater.* **2023**, 2201931, <https://doi.org/10.1002/adem.202201931>.
- [2] H. K. D. H. Bhadeshia, *Bainite in Steels: Transformations, Microstructure and Properties*, 2nd ed, IOM Communications, London **2001**.
- [3] F. G. Caballero, M. K. Miller, C. Garcia-Mateo, *Mater. Chem. Phys.* **2014**, 146, 50.
- [4] H. K. D. H. Bhadeshia, D. V. Edmonds, *Met. Sci.* **1983**, 17, 411.
- [5] F. G. Caballero, H. Roelofs, S. Hasler, C. Capdevila, J. Chao, J. Cornide, C. Garcia-Mateo, *Mater. Sci. Technol.* **2012**, 28, 95.
- [6] E. Kozeschni, H. K. D. H. Bhadeshia, *Mater. Sci. Technol.* **2008**, 24, 343.
- [7] B. P. J. Sandvik, *Metall. Mater. Trans. A* **1982**, 13, 777.
- [8] F. G. Caballero, C. Garcia-Mateo, J. Chao, M. J. Santofimia, C. Capdevila, C. G. de Andrés, *ISIJ Int.* **2008**, 48, 1256.
- [9] C. Hofer, H. Leitner, F. Winkelhofer, H. Clemens, S. Primig, *Mater. Charact.* **2015**, 102, 85.
- [10] C. Hofer, S. Primig, H. Clemens, F. Winkelhofer, R. Schnitzer, *Adv. Eng. Mater.* **2017**, 19, 1600658.
- [11] C. Garcia-Mateo, F. G. Caballero, *Mater. Trans.* **2005**, 46, 1839.
- [12] M. Abareschi, E. Emadoddin, *Mater. Des.* **2011**, 32, 5099.
- [13] G. Gao, R. Liu, K. Wang, X. Gui, R. Misra, B. Bai, *Scr. Mater.* **2020**, 184, 12.
- [14] H. Bhadeshia, D. V. Edmonds, *Acta Metall.* **1980**, 28, 1265.
- [15] B. P. J. Sandvik, H. P. Nevalainen, *Met. Technol.* **1981**, 8, 213.
- [16] I. Mueller, R. Rementeria, F. G. Caballero, M. Kuntz, T. Sourmail, E. Kerscher, *Materials* **2016**, 9, 831.
- [17] M. C. Marinelli, I. Alvarez-Armas, U. Krupp, *Mater. Sci. Eng., A* **2017**, 684, 254.
- [18] R. Rementeria, L. Morales-Rivas, M. Kuntz, C. Garcia-Mateo, E. Kerscher, T. Sourmail, F. G. Caballero, *Mater. Sci. Eng., A* **2015**, 630, 71.
- [19] X. Long, F. Zhang, Z. Yang, B. Lv, *Mater. Sci. Eng., A* **2018**, 715, 10.
- [20] Y. Fan, X. Gui, M. Liu, X. Wang, C. Feng, G. Gao, *Metals* **2022**, 12, 856.
- [21] Q. Zhou, L. Qian, J. Meng, L. Zhao, F. Zhang, *Mater. Des.* **2015**, 85, 487.
- [22] W. J. Dixon, *J. Am. Stat. Assoc.* **1965**, 60, 967.
- [23] W. J. Dixon, A. M. Mood, *J. Am. Stat. Assoc.* **1948**, 43, 109.
- [24] R. Morrissey, T. Nicholas, *Int. J. Fatigue* **2006**, 28, 1577.
- [25] C. Müller, M. Wächter, R. Masendorf, A. Esderts, *Int. J. Fatigue* **2017**, 100, 296.
- [26] C. F. C. Bandeira, P. P. Kenedi, J. T. P. de Castro, *Lat. Am. J. Solids Struct.* **2018**, 15, <https://www.doi.org/10.1590/1679-78254331>.
- [27] R. de Finis, D. Palumbo, F. Ancona, U. Galiotti, *Int. J. Fatigue* **2015**, 74, 88.
- [28] K. Hayabusa, K. Inaba, H. Ikeda, K. Kishimoto, *Exp. Mech.* **2017**, 57, 185.
- [29] G. La Rosa, *Int. J. Fatigue* **2000**, 22, 65.
- [30] L. Zhang, X. S. Liu, S. H. Wu, Z. Q. Ma, H. Y. Fang, *Int. J. Fatigue* **2013**, 54, 1.
- [31] F. Walther, *Mater. Test.* **2014**, 56, 519.
- [32] F. Walther, D. Eifler, *Mater. Sci. Eng., A* **2007**, 468–470, 259.
- [33] A. Baqerzadeh Chehreh, M. Grätzl, J. P. Bergmann, F. Walther, *Metals* **2020**, 10, 1510.
- [34] F. Niessen, T. Nyssönen, A. A. Gazder, R. Hielscher, *J. Appl. Crystallogr.* **2022**, 55, 180.
- [35] S. Ramesh Babu, T. P. Davis, T. Haas, A. Jarvenpää, J. Kömi, D. Porter, *Metals* **2020**, 10, 171.
- [36] E. R. Davies, *Computer and Machine Vision: Theory, Algorithms, Practicalities*, Academic Press, Waltham, MA, **2012**.
- [37] M. Ackermann, D. Iren, S. Wesselmecking, D. Shetty, U. Krupp, *Mater. Charact.* **2022**, 191, 112091.
- [38] M. Ferrari, L. Lutterotti, *J. Appl. Phys.* **1994**, 76, 7246.
- [39] H. Bhadeshia, *Acta Metall.* **1980**, 28, 1103.
- [40] C. Hofer, F. Winkelhofer, H. Clemens, S. Primig, *Mater. Sci. Eng., A* **2016**, 664, 236.
- [41] X. Y. Long, F. C. Zhang, J. Kang, Z. N. Yang, D. D. Wu, K. M. Wu, G. H. Zhang, *Mater. Sci. Technol.* **2017**, 33, 615.
- [42] M. Morawiec, V. Ruiz-Jimenez, C. Garcia-Mateo, J. A. Jimenez, A. Grajcar, *Arch. Civ. Mech. Eng.* **2022**, 22, 152.
- [43] J. Meng, Y. Feng, Q. Zhou, L. Zhao, F. Zhang, L. Qian, *J. Mater. Eng. Perform.* **2015**, 24, 3068.
- [44] L. C. Chang, H. K. D. H. Bhadeshia, *Mater. Sci. Technol.* **1995**, 11, 874.
- [45] E. Swallow, H. K. D. H. Bhadeshia, *Mater. Sci. Technol.* **1996**, 12, 121.
- [46] H. Guo, X. Feng, A. Zhao, Q. Li, M. Chai, *J. Mater. Res. Technol.* **2020**, 9, 1593.
- [47] J. Cornide, C. Garcia-Mateo, C. Capdevila, F. G. Caballero, *J. Alloys Compd.* **2013**, 577, S43.
- [48] K. Wang, Z. Tan, G. Gao, B. Gao, X. Gui, R. Misra, B. Bai, *Mater. Sci. Eng., A* **2016**, 675, 120.
- [49] J. C. Pang, S. X. Li, Z. G. Wang, Z. F. Zhang, *Mater. Sci. Eng., A* **2013**, 564, 331.
- [50] J. C. Pang, S. X. Li, Z. G. Wang, Z. F. Zhang, *Fatigue Fract. Eng. Mater. Struct.* **2014**, 37, 958.
- [51] U. Krupp, C. West, H.-J. Christ, *Mater. Sci. Eng., A* **2008**, 481–482, 713.
- [52] C. Y. Huo, H. L. Gao, *Mater. Charact.* **2005**, 55, 12.
- [53] S. D. Antolovich, B. Singh, *Metall. Trans.* **1971**, 2, 2135.
- [54] X. Y. Qi, L. X. Du, J. Hu, R. Misra, *Mater. Sci. Eng., A* **2018**, 718, 477.

- [55] E. R. Parker, V. F. Zackay, *Eng. Fract. Mech.* **1973**, 5, 147.  
[56] K. Hussain, *Eng. Fract. Mech.* **1997**, 58, 327.  
[57] U. Krupp, *Fatigue Crack Propagation in Metals and Alloys: Microstructural Aspects and Modelling Concepts*, John Wiley distributor; Wiley-VCH, Chichester; Weinheim **2007**.  
[58] Y. Yu, J. L. Gu, L. Xu, F. L. Shou, B. Z. Bai, Y. B. Liu, *Mater. Des.* **2010**, 31, 3067.  
[59] A. Kozłowska, A. Grajcar, A. Janik, K. Radwański, U. Krupp, K. Matus, M. Morawiec, *Archiv. Civ. Mech. Eng.* **2021**, 21, 133.  
[60] I. Nikitin, M. Besel, *Int. J. Fatigue* **2008**, 30, 2044.